energies
MDPI

Article

Dynamic Modeling and Robust Controllers Design for Doubly Fed Induction Generator-Based Wind Turbines under Unbalanced Grid Fault Conditions

Imran Khan [1], Kamran Zeb [1,2], Waqar Ud Din [1], Saif Ul Islam [1], Muhammad Ishfaq [1], Sadam Hussain [1] and Hee-Je Kim [1,*]

[1] School of Electrical Engineering, Pusan National University, San 30, ChangJeon 2 Dong, Pusandaehak-ro 63 beon-gil 2, Geumjeong-gu, Busan 46241, Korea; imrankhan@pusan.ac.kr (I.K.); kami_zeb@yahoo.com (K.Z.); waqudn@pusan.ac.kr (W.U.D.); shaheen_575@yahoo.com (S.U.I.); engrishfaq1994@gmail.com (M.I.); sadamengr15@gmail.com (S.H.)

[2] School of Electrical Engineering and Computer Science, National University of Sciences and Technology, Islamabad 44000, Pakistan

* Correspondence: heeje@pusan.ac.kr; Tel.: +82-10-3462-1990

Received: 16 December 2018; Accepted: 30 January 2019; Published: 31 January 2019

Abstract: High penetration of large capacity wind turbines into power grid has led to serious concern about its influence on the dynamic behaviors of the power system. Unbalanced grid voltage causing DC-voltage fluctuations and DC-link capacitor large harmonic current which results in degrading reliability and lifespan of capacitor used in voltage source converter. Furthermore, due to magnetic saturation in the generator and non-linear loads distorted active and reactive power delivered to the grid, violating grid code. This paper provides a detailed investigation of dynamic behavior and transient characteristics of Doubly Fed Induction Generator (DFIG) during grid faults and voltage sags. It also presents novel grid side controllers, Adaptive Proportional Integral Controller (API) and Proportional Resonant with Resonant Harmonic Compensator (PR+RHC) which eliminate the negative impact of unbalanced grid voltage on the DC-capacitor as well as achieving harmonic filtering by compensating harmonics which improve power quality. Proposed algorithm focuses on mitigation of harmonic currents and voltage fluctuation in DC-capacitor making capacitor more reliable under transient grid conditions as well as distorted active and reactive power delivered to the electric grid. MATLAB/Simulink simulation of 2 MW DFIG model with 1150 V DC-linked voltage has been considered for validating the effectiveness of proposed control algorithms. The proposed controllers performance authenticates robust, ripples free, and fault-tolerant capability. In addition, performance indices and Total Harmonic Distortions (THD) are also calculated to verify the robustness of the designed controller.

Keywords: Wind Turbine (WT); Doubly Fed Induction Generator (DFIG); unbalanced grid voltage; DC-linked voltage control; Proportional Resonant with Resonant Harmonic Compensator (PR+HC) controller; Adaptive Proportional Integral (API) control; power control

1. Introduction

Extinction and environmental concerns regarding the use of fossil fuels for power generation have shifted the attention of scientists towards Renewable Energy (RE). Among all RE resources, wind power generation has recorded significant growth in the last decade. With energy saving ambitions, by 2030 wind power will be able to supply 29.1% of the electricity needed worldwide and 34.5% by 2050 [1,2]. Energy quality is a significant feature in grid-connected converters, and wind power generators have a high influence on the stability and security of the power grid. To meet the required results, WT systems must be continuously developed and their performance improved. In recent years, DFIG based WT have become a well-known and widely installed due to their high efficiency, variable speed operation (±33% around the synchronous speed), four quadrant active and reactive power capability, less power losses, small converter rating (around 30% of generator rating), reduced mechanical stress and hence minimized pulsating power and torque [3–6].

Since the DFIG stator and the grid are connected directly, during unbalanced grid voltage conditions a negative sequence is added to stator flux, resulting in a flow of large negative sequential currents in the rotor and stator causing second-order harmonic fluctuating power and electromagnetic torque [7,8]. From both the Rotor Side Converter (RSC) and Grid Side Converter (GSC), active power fluctuations flow through DC-linked capacitors as shown in Figure 1. resulting in voltage ripples in the DC-link capacitor as well as significant second-order harmonic currents in the DC-capacitor [9], which affect the DC-capacitor causing high power losses and increased operational temperature which may evaporate the electrolyte faster making their lifespan shorter. In addition, fluctuations in torque can cause wear and tear of mechanical parts such as the shaft and gear box [10]. Further, a comparison of the high and low frequency ripple currents shows that ripple currents with low frequency are more detrimental [11,12]. Hence, voltage ripples and converter DC-linked capacitor with large low frequency currents under unbalanced conditions are the most serious issues of DFIG [8,9]. Under the unbalanced condition the DC-voltage control in GSC differs slightly from the GSC for the DFIG, because the DC-voltage ripples are not only caused by the unbalanced grid voltage, but also by RSC fluctuating active power. These two disturbances i.e., active power fluctuation of RSC and unbalanced grid voltage, should be rejected by GSC to ensure a constant DC-voltage.

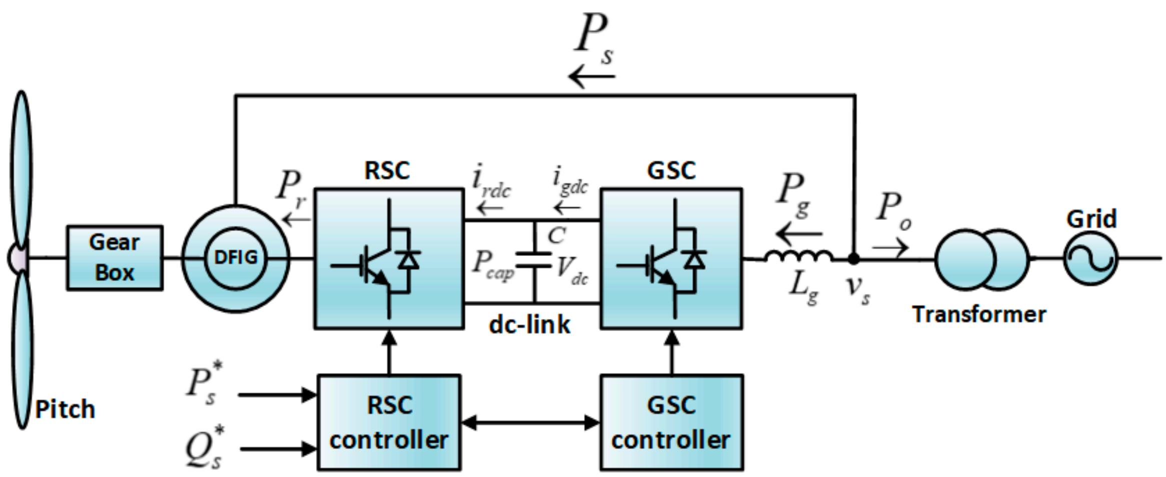

Figure 1. Active power flow in a DFIG wind turbine.

Numerous control strategies have been presented to decrease the voltage ripple for GSC controllers under unbalanced voltage conditions. To regulate negative sequence current and positive currents at the same time dual current control methods were designed [9,13–15]. Grid voltage and the desired power ensure the calculation of negative and positive reference currents. By setting of the references multiple control targets are available, like constant DC voltage, constant electromagnetic power, constant stator power and balanced stator currents [14,15]. The GSC fluctuating active power output must be equal to that of RSC under unbalanced conditions. Then the GSC reference current depends on the RSC fluctuating active power [9,14]. Consequently, implementation of dual current control method is not applicable in modular structural wind power converters. Another method to reduce voltage ripples during unbalance grid voltage conditions is feed-forward control which comprising RSC DC-current feed-forward control [16–19] and grid voltage feedforward control [20,21]. Feed-forward control for RSC DC-current reduces the impact of fluctuating RSC active power while feed-forward control for grid voltage reduces the impact on DC-capacitor due to unbalanced grid voltages.

The feed-forward technique control performance may be degraded by the control delay, which results in an addition of high-frequency noise to the feed-forward term. Moreover, additional hardware of the load current detection may require detecting the DC current of the RSC [17,18]. An alternate approach is used to get rid of additional detection circuits, whereby the RSC real-time active power is calculated by GSC based on rotor voltage reference and rotor current [16,19] which require integration of both the RSC controller and GSC controller into a single controller. This integration results in loss of the modular structure of DFIG converters. For high maintenance and reliability, DFIG converter exhibits modularity which is not achieved in this technique Automatic generation control employed with inertia support for load frequency control was analyzed in an interconnected multigeneration wind power system [22]. For mitigation of subsynchronous resonance, a non-linear damping controller was designed using a partial feed-back linearization technique in series compensated DFIG-based wind farms [23]. To mitigate subsynchronous resonance (SSR) oscillations, doubly fed induction generator (DFIG) supplemental control is used [24], in which a supplemental signal is introduced into the control loop of the DFIG voltage source converter. Furthermore, two-degree-of -freedom along with a damping control loop is used [25] to mitigate SSR which is caused by induction generator effects and thus enhance the system stability. In [26] two SSR oscillation mitigating strategies were compared, which generate supplementary damping control signal; integrated on the rotor side converter and grid side converter. A hybrid scheme for enhancing fault ride through capability of DFIG under symmetric and asymmetric faults was presented [27], comprising an energy storage system, break chopper and switch type fault current limiter.

The main contributions of this paper may be summarized as follows:

(1) A simplified and comprehensive study about dynamics characteristics and modelling of DFIG based grid connected wind turbine system is presented.
(2) Active and reactive power stability and elimination of voltage fluctuation and harmonic current of DC-capacitor using API and PR+RHC as a grid side control algorithm are discussed.
(3) A comprehensive performance analysis under normal condition and various faults, i.e.: Under Voltage, Over Voltage, Single Phase, and Double Phase faults conditions to validate the active power, reactive power, and DC-link voltage performance of the proposed API and PR+RHC controllers is performed.
(4) A comparative assessment of designed controllers such as API and PR+RHC with a conventionally tuned PI controller is also carried out.
(5) A FFT analysis of a PI controller, and the proposed API and PR+RHC controller by calculating the total harmonics distortion of grid current to validate the robustness of proposed PR controller is presented.
(6) The performance of various controllers (PI, API & PR+RHC) was evaluated by calculating three control parameters i-e. Integral Absolute Error (IAE), Integral Square Error (ISE) and Integral Time-weighted Absolute Error (ITAE) which precisely compare their performances.

The remaining paper is organized as follows: in Section 2, detailed modeling of DFIG is discussed. The proposed WTs model is explained in Section 3. The proposed API and PR+RHC controllers are designed in Section 4. Results and discussion are presented in Section 5. The paper is concluded in Section 6.

2. Modeling of DFIG

The configuration of a DFIG-based wind turbine is illustrated in Figure 1. The stator and grid voltage are directly linked to each other while the rotor and back-to-back converter are interfaced, comprising a GSC common DC-link and a RSC [28]. The generator output power is controlled by the RSC while GSC ensures the stability of the DC-link voltage irrespective of the direction and magnitude of the rotor power [29]. At the wind turbine the terminal grid active power P_O is equal to the sum of the stator active power P_s and the grid active power P_g. The current and power reference directions are shown in Figure 1. The equivalent circuit of DFIG is shown in a *dq*-synchronous reference frame in Figure 2.

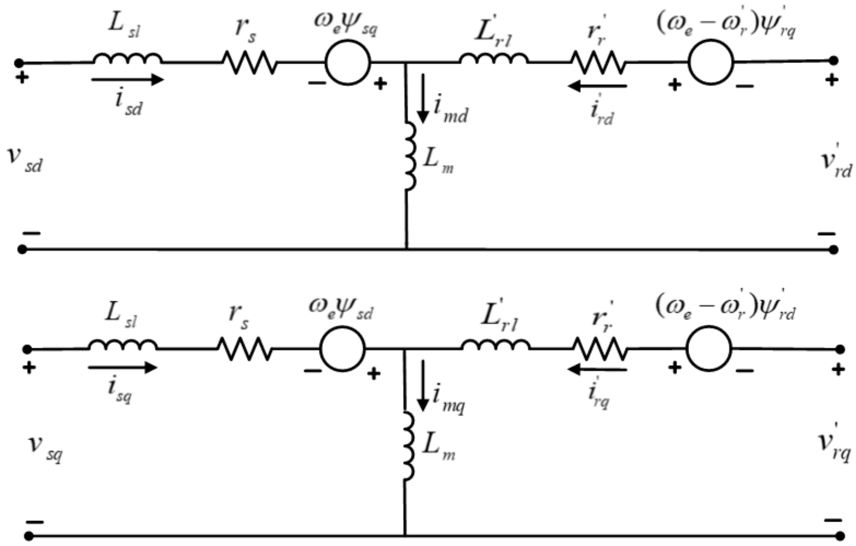

Figure 2. Equivalent circuit of the DFIG in the *dq*-synchronous reference frame.

The DFIG mathematical model is analyzed in the *dq* reference frame and is defined by Equations (1) to (6) [30,31]:

$$\left.\begin{aligned} v_{sd} &= r_s i_{sd} + \tfrac{d\psi_{sd}}{dt} - \omega_e \psi_{sq} \\ v_{sq} &= r_s i_{sq} + \tfrac{d\psi_{sq}}{dt} + \omega_e \psi_{sd} \end{aligned}\right\} \tag{1}$$

$$\left.\begin{aligned} v'_{rd} &= r'_r i'_{rd} + \tfrac{d\psi'_{rd}}{dt} - \omega_{sl} \psi'_{rq} \\ v'_{rq} &= r'_r i'_{rq} + \tfrac{d\psi'_{rq}}{dt} - \omega_{sl} \psi'_{rd} \end{aligned}\right\} \tag{2}$$

$$\omega_{sl} = \omega_e - \omega'_r \tag{3}$$

$$\left.\begin{aligned} \psi_{sd} &= L_s i_{sd} + L_m i'_{rd} \\ \psi_{sq} &= L_s i_{sq} + L_m i'_{rq} \end{aligned}\right\} \tag{4}$$

$$\left.\begin{aligned} \psi'_{rd} &= L'_r i'_{rd} + L_m i_{sd} \\ \psi'_{rq} &= L'_r i'_{rq} + L_m i_{sq} \end{aligned}\right\} \tag{5}$$

$$\left.\begin{aligned} L_s &= L_{sl} + L_m \\ L'_r &= L'_{rl} + L_m \end{aligned}\right\} \tag{6}$$

where V_{sd}, V_{sq} and V'_{rd}, V'_{rq} are the stator and rotor voltages in the *dq* reference frame, r_s and r'_r are the stator and rotor per phase electrical resistances, i_{sd}, i_{sq} and i'_{rd}, i'_{rq} are stator and rotor currents in the *d-q* reference frame, ψ_{sd}, ψ_{sq} and ψ'_{rd}, ψ'_{rq} are stator and rotor fluxes in the *dq* reference frame, L_s, L'_r and L_m are stator, rotor and magnetizing per phase inductances, L_{sl} and L'_{rl} are stator and rotor leakage inductance, ω_e and ω'_r are the synchronous and rotor speeds.

The magnetic flux in the stator in *d* and *q* axis is determined by Equation (7) and it is assumed that all magnetic fluxes are aligned with the *d* axis:

$$\left.\begin{aligned} \psi_{sq} = 0 \quad & and \ \tfrac{d\psi_{sq}}{dt} = 0 \\ \psi_s = \psi_{sd} = L_m i_{ms} \quad & and \ \tfrac{d\psi_{sq}}{dt} = 0 \end{aligned}\right\} \tag{7}$$

The DFIG stator active and reactive power are computed for rotor side after simplification as:

$$P_s = -\frac{3}{2}\frac{L_m}{L_s} v_s i'_{rq} \tag{8}$$

$$Q_s = \frac{3}{2}\frac{L_m}{L_s} v_s \left(\frac{v_s}{(\omega_e L)_m} - i'_{rd} \right) \tag{9}$$

From Equations (8) and (9), one observes that the active and reactive powers can be controlled by the quadrature components of rotor current, considering the constant voltage. The converter controls the active and reactive powers of the DFIG stator, where $1 - L_m^2/L_s L'_r$ and i_{ms} is the magnetizing current.

The GSC block diagram uses current loops to i_d and i_q, having i_d^* as reference from the DC-link. Since i_q^* = 0, the converter operates at a unity power factor. The reference signal generator produces the current reference (i_d^*, i_q^*), from Equations (10) and (11):

$$P_{ref} = \frac{3}{2}[v_d i_d^*] \tag{10}$$

$$Q_{ref} = \frac{3}{2}[v_q i_d^*] \tag{11}$$

3. Proposed Model

An overview of the control structure of a wind turbine system (WTS) [4,32,33] is shown in Figure 3. For maximum power extraction, the generator is controlled by a power converter, thereafter electrical parameters are generated based on generator and control algorithm while the generator torque ω_m is obtained from the turbine model [30].

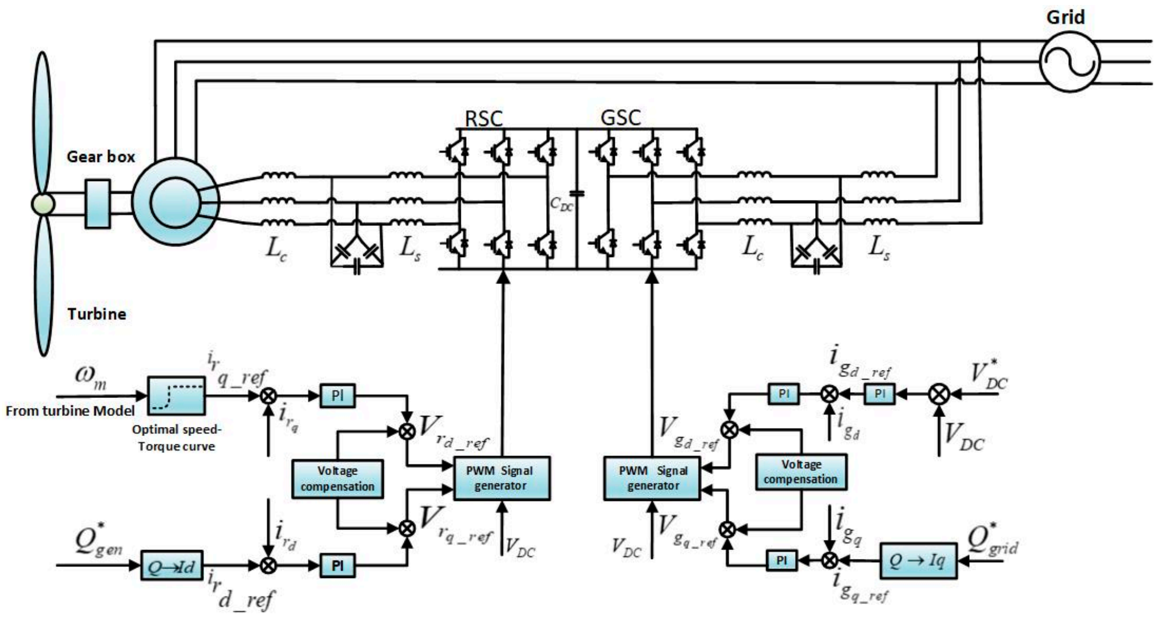

Figure 3. Control schematics for a DFIG wind turbine.

The electric and control models are classified into grid side and generator side as shown in Figure 3. The generator side control deals with two parameters, generator current and the duty cycle. DC-linked voltage alone with these two parameters is used to model generator side converters using the following Equations (12) and (13):

$$V_{s_{dq}} = D_{dq} \times V_{DC} \tag{12}$$

$$I_{dc} = D_d \times I_{s_d} \times D_q \times I_{s_q} \tag{13}$$

where D is the duty ratio, V_{DC} is the DC-link voltage, I_{DC} is the current flow into DC link, I_s is the stator current V_s is the stator voltage.

Based on the vector control of generator the control algorithm implemented here is for maximum power extraction. The control structure works in the following sequence: first in the reference current generation phase, the rotor's rotational speed is measured which is used to generate the reference torque from the maximum power/torque curve based on the turbine design and characteristic. Using this reference torque, a reference current signal is generated for the generator-side converter in the *dq* frame. In the current control loop phase, an error signal is generated by comparing the generated reference current and the measured current in the *dq* reference frame, which then generate a voltage reference for the converter by feeding through Proportional Integral (PI) controllers. In the modulation phase, the resulting reference voltages should be converted into a duty ratio for the generator side converter, and finally this will result in a PWM switching signal for the converter as shown in Figure 4.

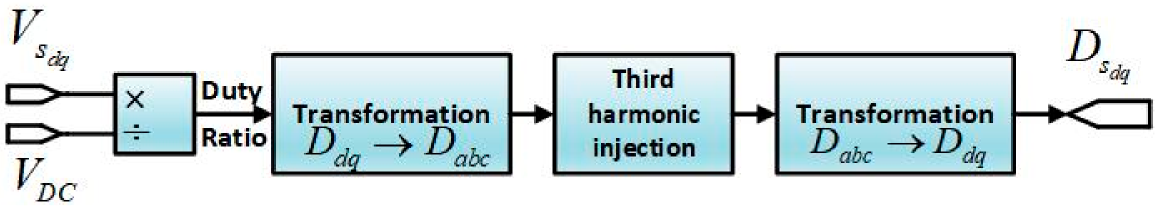

Figure 4. Modulation of generator-side converter in proposed model.

The converter model on the grid-side is elaborated by three differential Equations (14)–(16), which use the voltage of the grid and the resistance and inductance of the grid-side filter as input:

$$L_f \frac{di_{g_d}}{dt} + R_f i_{g_d} = \omega L_f i_{g_q} + V_{conv_d} - V_{grid_d} \tag{14}$$

$$L_f \frac{di_{g_q}}{dt} + R_f i_{g_q} = -\omega L_f i_{g_d} + V_{conv_q} - V_{grid_q} \tag{15}$$

$$C_{DC} \frac{dV_{DC}}{dt} = i_{DC} - k\left(i_{g_d} D_d + i_{g_q} D_q\right) \tag{16}$$

where the k value is dependent on the transformation technique used to convert *abc* values to *dq* values. The k value must be 1 is when using a normalized Clarke transformation and in case of a non-normalized transformation $k = 3/2$. Further, V_{DC} is the DC-link voltage, i_g is the grid current, R_f is the filter resister, D is the duty cycle, C_{DC} is the DC-linked capacitor, L_f is inductance of filter and V_{grid} is the voltage of grid.

In the *dq* reference frame the grid-side converter is controlled with the grid voltage. The reactive power which is transferred to the grid is controlled by i_{g_q}. Similarly, by maintaining the DC-linked voltage real power transferred to the grid is regulated by i_{g_d} current. Both the generator-side as well as the grid-side controller have the same limiting algorithms and modulation techniques.

4. Controller Design

4.1. API Controller

Control of traditional processes always depends on creating a mathematical model of the required system. An expert system was established to mimic the behavior of a skilled human operator for those processes too complex to be mathematically modeled in real time. Fuzzy logic controller (FLC) engines use as expert system paradigm for automatic process control. In addition, intuition and heuristics knowledge are also included into the system. This feature ranked FLC high in application where the existing models are ill defined, complex and not adequately reliable. FLC can mainly be classified into four main parts: fuzzifier, rules, inference engine and de-fuzzifier [34] as illustrated in Figure 5:

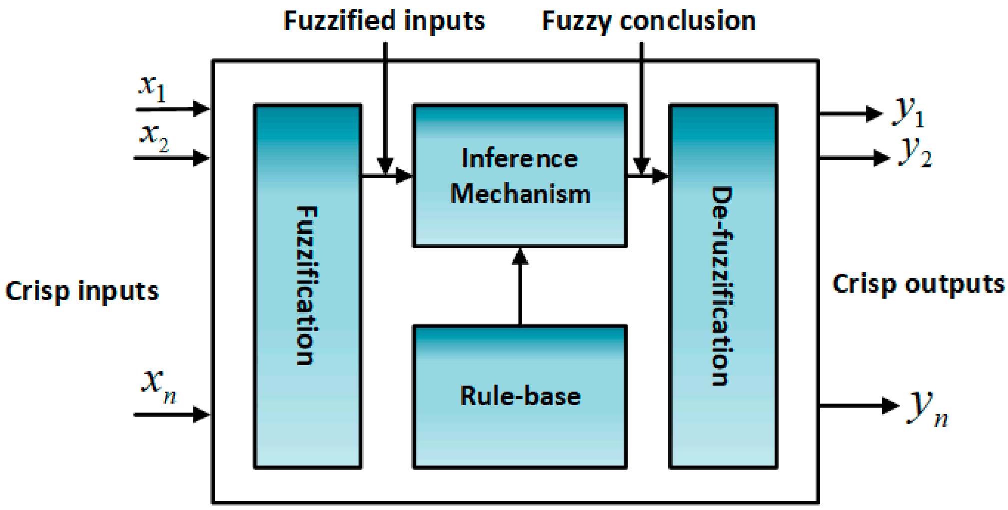

Figure 5. Fuzzy controller architecture.

4.2. Fuzzy PI Controller

The PI controller comprising constant integral and proportional gain k_i and k_p, respectively. Control scheme performance is enhanced by adaption of gain with respect to error. This distinguish feature of adaption can be achieved by applying fuzzy rules as illustrated in Table 1:

Table 1. Fuzzy rules.

Absolute Error ∣*e(t)*∣	Proportional Gain (k_p)	Integral Gain (k_i)
Zero	large	small
Small	large	zero
Large	large	large

Gaussian Member function (GMF) is applied here in the rules that needs two parameters i.e., center c_i and σ_i standard variance or deviation as:

$$\mu(x) = exp\left(-\frac{1}{2}\left(\frac{x_{i-c_i}}{\sigma_i}\right)^2\right) \tag{17}$$

Mathematical description of PI controller is illustrated as:

$$v_{dc}^*/i_{sd}^*/i_{sq}^*(PI) = k_p e(t) + k_i \int e(t)dt \tag{18}$$

where $v_{dc}^*/i_{sd}^*/i_{sq}^*$ is output of the controller, k_i and k_p is integral and proportional gain respectively and $e(t)$ is input of controller, furthermore PI controller gains are constant in the preceding equation that requires adaptation with respect to electrical fault perturbation, parameter uncertainties, load variation and load disturbances.

$$v_{dc}^*/i_{sd}^*/i_{sq}^*(Fuzzy) = F_1 k_1 e(t) + F_2 k_2 \int e(t)dt \tag{19}$$

where k_p and k_i results in fuzzy controller's output F_1 and F_2 respectively, and k_1 and k_2 are learning rates constant for k_p and k_i respectively as mentioned in Figure 6.

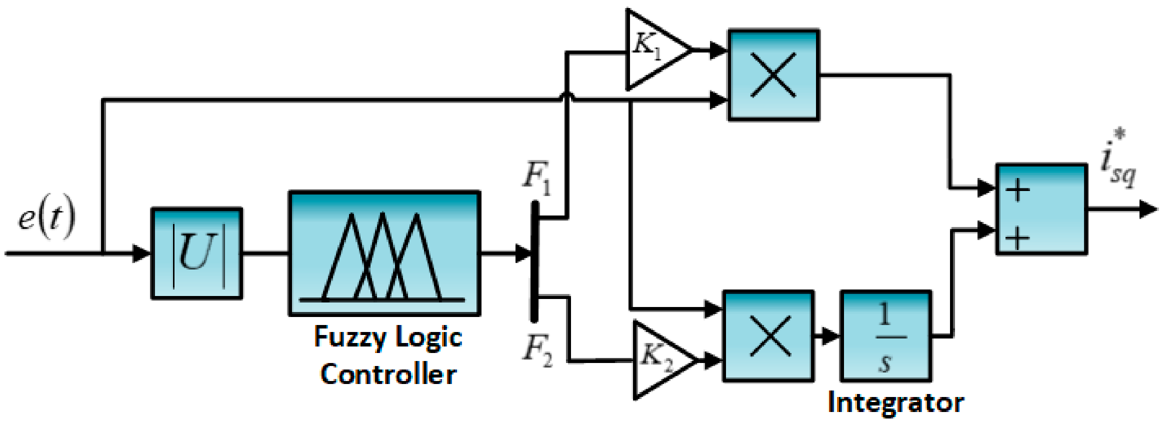

Figure 6. Adaptive PI controller.

A comparison of FLC-based adaptive PI control with PI conventionally tuned control as benchmark is provided in [35]. The gain for integral and proportional constant are calculated for the operating conditions by linearizing the system for numerous control loops.

4.3. Proportional Resonant Controller with Hormonic Compensator (PR+HC)

A PR controller has distinguished integration features. Due to the action of integration of frequencies near and around the resonance frequency; phase shift and static error do not occur in a PR controller. Although high order filters are used to obtain optimized current waves at the grid side during unbalanced grid conditions, in practical applications the current wave is not exactly the normal one, but has time varying elements of grid voltage with small deviations which result in poor THD of the feed-in current, but it is demanded in most grid standards [36,37] that the grid connected devices should be operated within certain frequencies range. To meet grid standards by improving the current quality a harmonic compensator is employed along with the PR controller as shown in Figure 7.

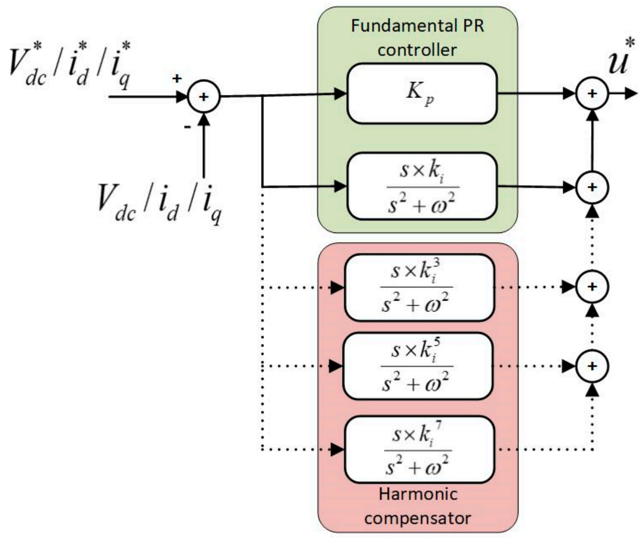

Figure 7. Combined structure of PR with harmonic compensator.

The PR controller consists of two parts i.e., proportional and resonant part, expressed by Equation (20) below:

$$G_{PR}(s) = K_p + K_i\left(\frac{S}{S^2+\omega^2}\right) \quad (20)$$

Here, ω is a resonant frequency. Due to the high gain at narrow band at the resonant frequency, PR can eliminate steady-state error. K_i is the time constant integral which is related to band width, and

K_p is proportional gain determines the phase of band width and gain of margin [38]. The harmonic compensator is parallelized with the PR controller for the sake of quality of grid current [39]. Harmonic compensators can be mathematically expressed as:

$$G_{HC}(s) = \sum_{h=3,5,7,\ldots} G_{HC}^{h}\ (s) \tag{21}$$

Here, $G_{HC}^{h}(s)$ is resonant controller with h^{th} order, where "h" is harmonic order. However, particularly

$$G_{HC}^{h}(s) = \frac{k_i^h\ s}{s^2 + (h\omega)^2} \tag{22}$$

where, k_i^h is the gain of particular order resonant controller.

5. Results and Discussion

To verify the proposed control strategies, a MATLAB/Simulink-based simulation have been carried out. The nominal parameters of the 2 MW system are listed in Table A1 (Appendix A). Control strategies (PI, API and PR+RHC) were simulated and compared under different conditions, i.e., rated, single-phase fault, two-phase fault, under-voltage, and over-voltage fault. The faults are applied for 200 ms which occurs from 1 s and cleared at 1.2 s, whereas the grid-side voltage was dropped and raised to 50% of its normal values in the under- and over-voltage cases, respectively. The performance of PI controller and proposed PR control strategy is evaluated by considering the following parameters: DC-linked voltage V_{dc}, stator voltage V_s, active current component I_d, reactive current component I_q, grid current Ig, rotor current I_r, rotor real power P_r, rotor voltage V_r, electro-magnetic torque T_{em}, stator real power P_s, stator reactive power P_{s_react}. Finally, THD and control performance measures are calculated to examine the controller's performance.

5.1. Rated Voltage

Conventional (PI) and Proposed (API & PR+RHC) control strategies are analyzed considering rated voltages. Figure 8a illustrates the DC-linked voltage responses of all control strategies; the PR+RHC and API controller responses are robust, faster and stabilize quickly, whereas the PI controller takes 1.3 s to attains stability. The API controller updates its parameters adoptively to minimize errors abruptly. The PR+RHC, due to the harmonic compensation, effectively tracks the reference, compared to PI. Figure 8b shows the rated stator voltage waveform for all control schemes. Figure 8c–e shows I_d for PI, API and PR+RHC control schemes, where both the designed controllers currents are efficiently tracking the reference currents. They have stable, robust, and chatter-free responses. The API and PR+RHC strategy responses for the rotor current are stable and less oscillatory with respect to the PI response as presented in Figure 8f. I_q is depicted in Figure 8g and the I_g response is illustrated for all controllers in Figure 8h. The API and PR+RHC response is faster and globally convergent. In case of P_s and P_r the API and (PR+RHC) controller responses are stable and robust, which reduces the acoustic noise, reduces stress on both drive trains and mechanical components which is a desired requirement as shown in Figure 8i,j. The T_{em} response is observed in Figure 8k, which shows minimum oscillation or almost stable responses for the API and PR+RHC control schemes, something that could be harmful from a mechanical view point. Figure 8l describes the P_{s_react} response which is quite stable and ripple less, which is desired in proposed control strategies. The rotor voltage response shows that API and PR+RHC strategies' responses are stable and less oscillatory with respect to the PI response as shown in Figure 8m. The performance indices of all the control schemes are evaluated in Tables 2–4 for V_{dc}, I_d, I_q, respectively. Three control measuring parameters, i.e., Integral Absolute Error (IAE), Integral Square Error (ISE) and Integral Time-weighted Absolute Error (ITAE) are calculated for all controllers which precisely compare their performances. The performance of a controller is based on its minimum value, where the smaller the value of parameters, the better the controller performance. In all three parameters API and PR+RHC controllers' values are the minimum compared with the PI controller, which proves the robust performance of the proposed controllers. Finally, the control schemes (PI, API & PR+RHC) are further investigated using FFT analysis of the grid current, which shows that the proposed API and PR+RHC strategies' grid currents are more robust and less harmonic with THD 0.02% and 0.06% respectively, as compared to 0.07% THD of the PI controller as shown in Figure 8n–p.

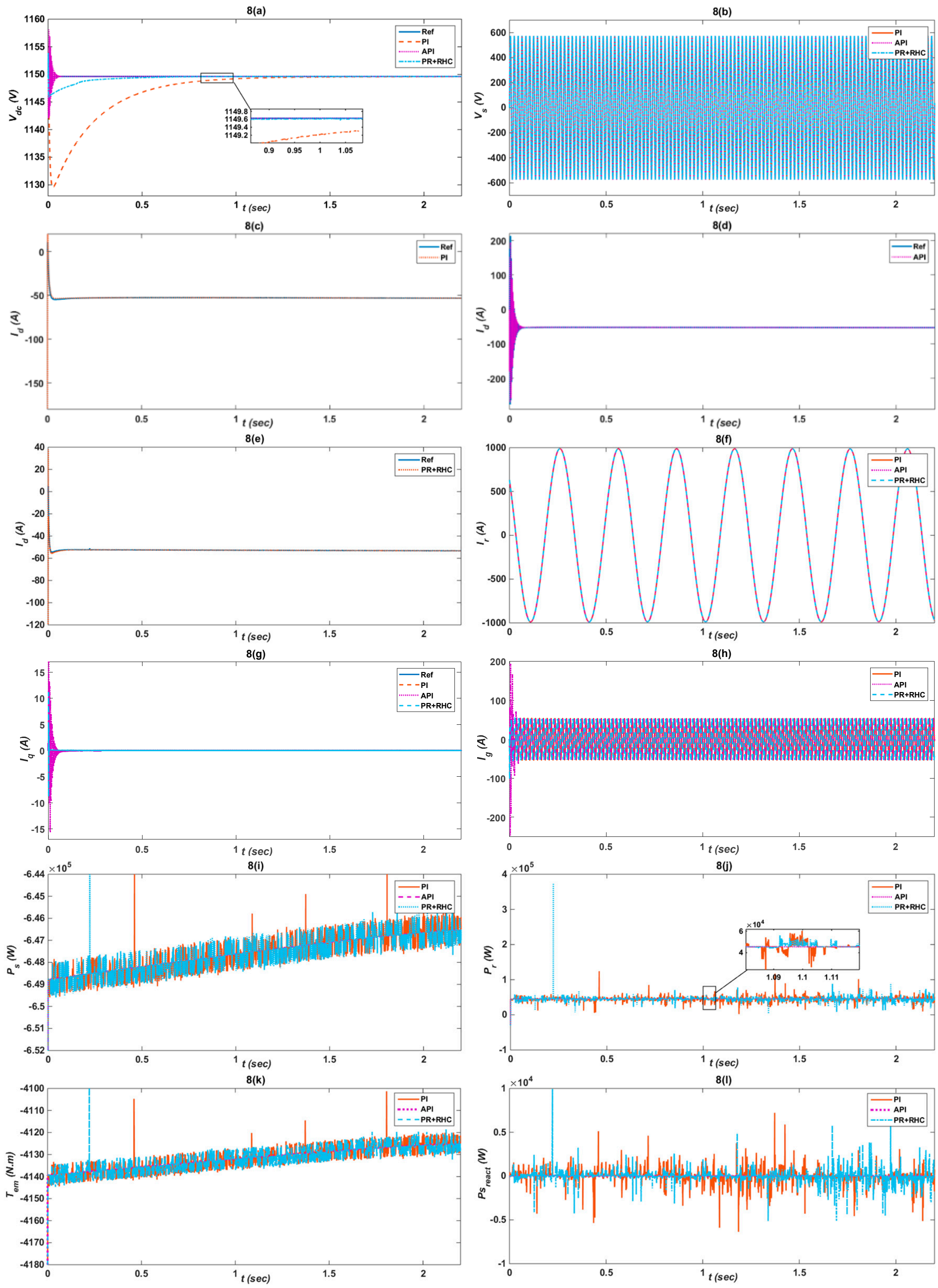

Figure 8. *Cont.*

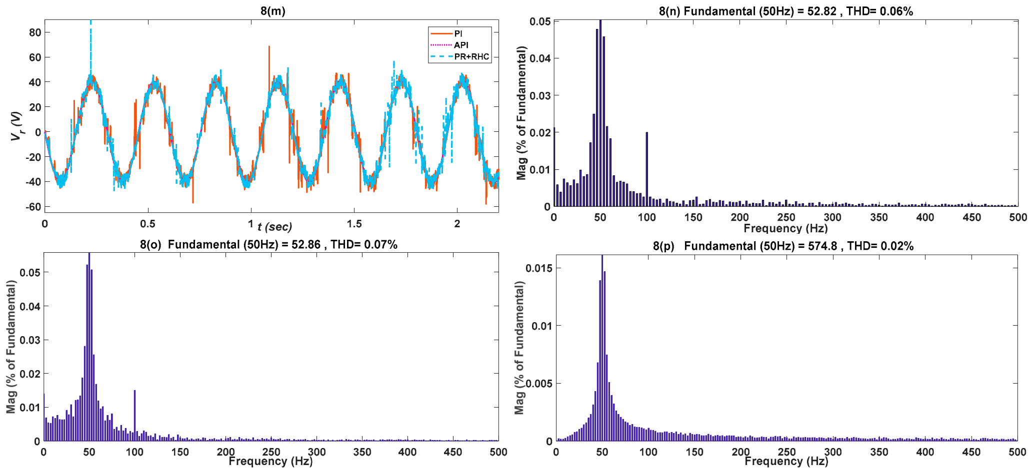

Figure 8. Comparison of PI and Proposed API and PR+RHC controllers responses under rated voltage, considering: (**a**) Dc-link voltage V_{dc}; (**b**) Stator voltage V_s; (**c**–**e**) Active component of current I_d; (**f**) Rotor current I_r; (**g**) Reactive component I_q; (**h**) Grid current I_g; (**i**) Stator active power P_s; (**j**) Rotor active power P_r; (**k**) Electromagnetic torque T_{em}; (**l**) Stator reactive power Ps_{react}; (**m**) Rotor voltage V_r; (**n**) PR+RHC controller THD; (**o**) PI controller THD; (**p**) API controller THD.

Table 2. Performance evaluation of designed control strategies for V_{dc}.

Control Strategies	Performance Index		
	IAE	ISE	ITAE
PI	5.473	55.95	1.991
API	0.1145	0.659	0.0810
PR+RHC	0.46	1.37	0.0325

Notes: IAE: Integral Absolute Error, ISE: Integral Square Error, ITAE: Integral of Time-Weighted Absolute Error.

Table 3. Performance evaluation of designed control strategies for I_d.

Control Strategies	Performance Index		
	IAE	ISE	ITAE
PI	2.50	20.78	0.0749
API	0.96	6.34	0.0224
PR+RHC	0.0117	5.68	0.0094

Notes: IAE: Integral Absolute Error, ISE: Integral Square Error, ITAE: Integral of Time-Weighted Absolute Error.

Table 4. Performance evaluation of designed control strategies for I_q.

Control Strategies	Performance Index		
	IAE	ISE	ITAE
PI	0.18	1.208	0.0066
API	0.01	0.062	0.0016
PR+RHC	0.017	0.069	0.004

Notes: IAE: Integral Absolute Error, ISE: Integral Square Error, ITAE: Integral of Time-Weighted Absolute Error.

5.2. Under-Voltage

The grid voltage is dropped to 50% of its rated value for 200 ms from 1 s to 1.2 s during the under-voltage case, as illustrated in Figure 9b. The proposed controller V_{dc} response, shown in Figure 9a, is less oscillatory, fast, and robust for the API and PR+RHC algorithms, as compared to PI's response which is unstable and out of limits. Figure 9c–e clearly shows that I_d completely traces the reference value which indicates the robustness of the proposed (API & PR+RHC) strategies. The API controller updates its parameters using fuzzy rules to track the reference abruptly and the PR+RHC, due to its harmonic compensation, effectively minimizes the error, in comparison to the PI controller. The proposed controller responses in the case of I_r is shown in Figure 9f. Figure 9g depicts I_q having smooth response for the proposed controllers which gain stability soon after voltage the reaches a normal value. Figure 9h illustrates the I_g response for the API & (PR+RHC) controllers with respect to the PI controller which ensures grid stability. The P_r and P_s responses are described in Figure 9i,j which show that the API & (PR+RHC) controller responses are less oscillatory, and more stable as compared to the PI controller which reduces mechanical stress y as well as stress on drives.

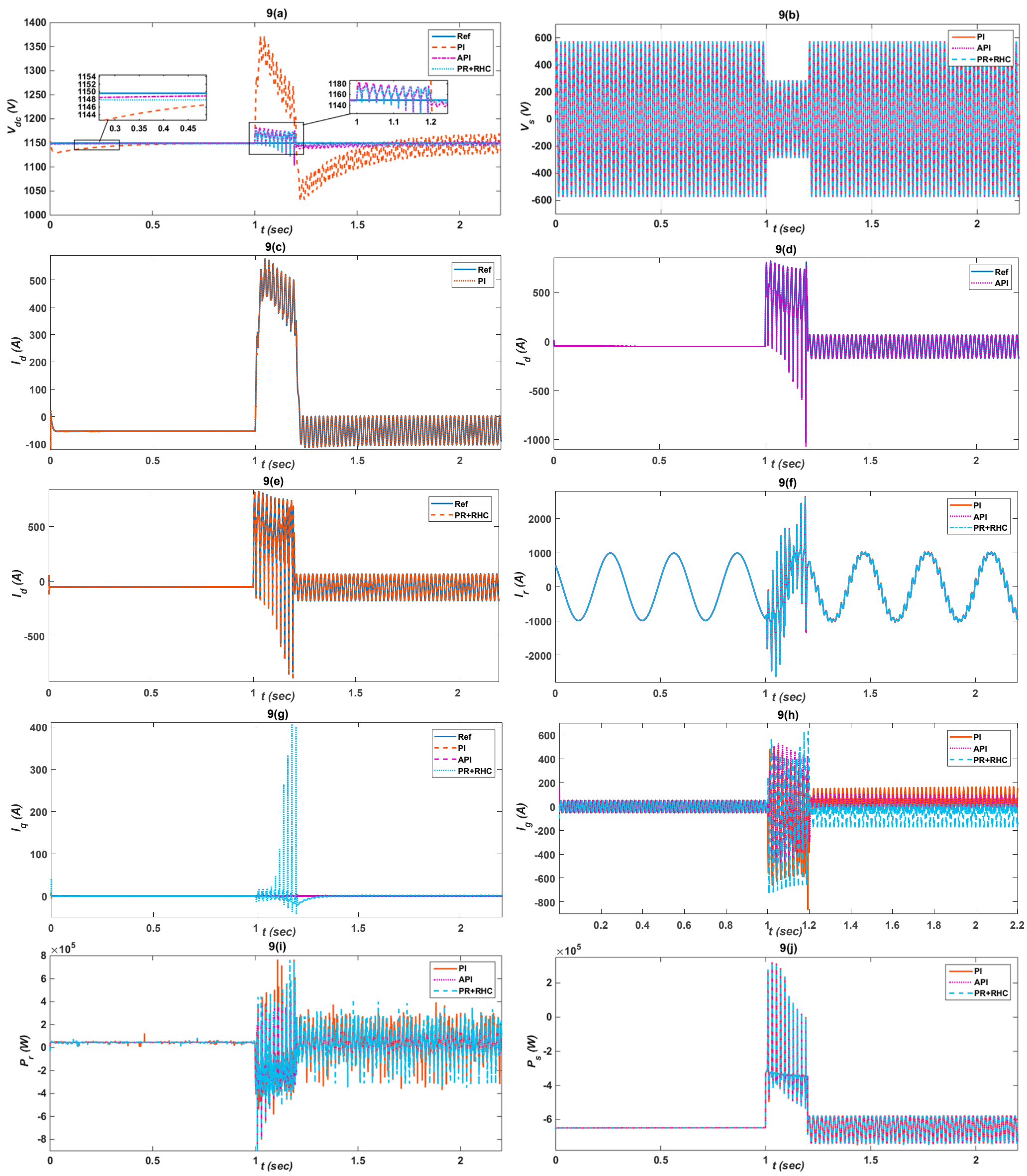

Figure 9. *Cont.*

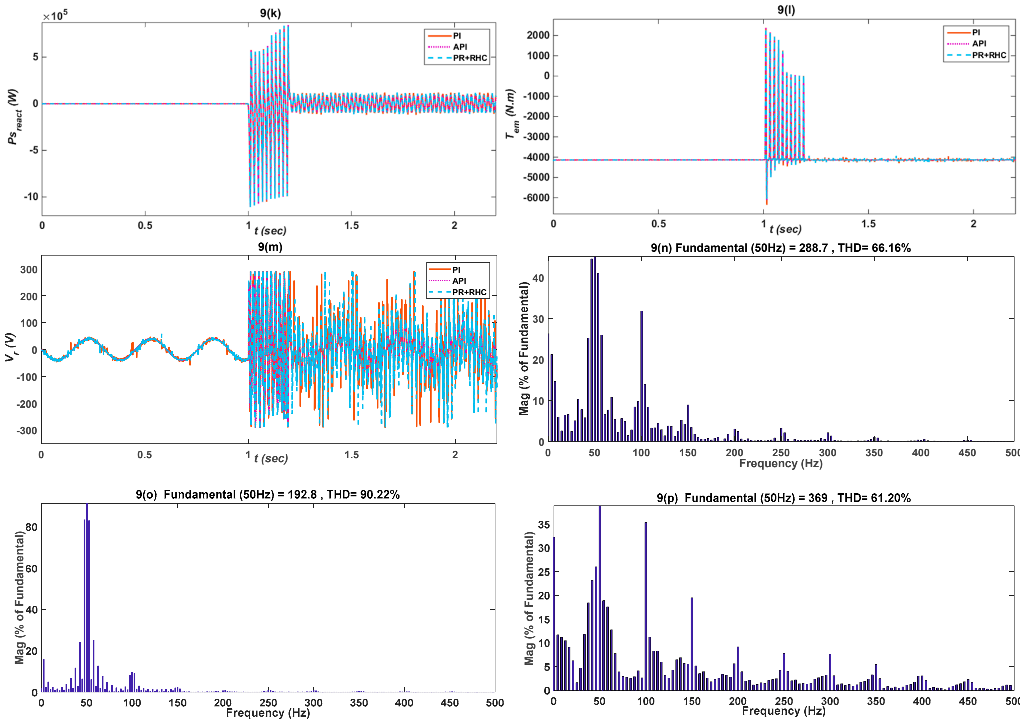

Figure 9. Comparison of PI and Proposed API and PR+RHC controller responses under undervoltage fault considering: (**a**) Dc-link voltage V_{dc}; (**b**) Stator voltage V_s; (**c**–**e**) Active component of current I_d; (**f**) Rotor current I_r; (**g**) Reactive component I_q; (**h**) Grid current I_g; (**i**) Rotor active power P_r; (**j**) Stator active power P_s; (**k**) Electromagnetic torque T_{em}; (**l**) Stator reactive power Ps_{react}; (**m**)Rotor voltage V_r; (**n**) PR+RHC controller THD; (**o**) PI controller THD; (**p**) API controller THD.

The Ps_{react}, T_{em} and V_r responses for both the proposed and conventional strategy are shown in in Figure 9k–m. Finally, the robustness of the proposed controllers over the PI conventional controller was proved by harmonic spectrum analysis of I_g, The THD value for the PI controller was 90.22% which is reduced to 61.20% and 66.16% in the case of the API and PR+RHC, respectively, and demonstrated in Figure 9n–p. The performance indices of all the control schemes are evaluated in Tables 5–7 for V_{dc}, I_d, and I_q, respectively. In the case of the API & PR+RHC controllers, all three parameter values are the minimum compared with the PI controller, which proves the better performance of the proposed controllers in under-voltage conditions.

Table 5. Performance evaluation of the designed control strategies for V_{dc}.

Control Strategies	Performance Index		
	IAE	ISE	ITAE
PI	99.7	6240	211.8
API	16.2	120.8	37.46
PR+RHC	13.36	98.36	29.90

Table 6. Performance evaluation of the designed control strategies for I_d.

Control Strategies	Performance Index		
	IAE	ISE	ITAE
PI	18.74	583.4	53.43
API	3.015	142.1	5.431
PR+RHC	4.59	154.26	6.55

Table 7. Performance evaluation of the designed control strategies for I_q.

Control Strategies	Performance Index		
	IAE	ISE	ITAE
PI	1.601	0.8957	4.672
API	0.0019	0.0021	0.0024
PR+RHC	0.026	0.102	0.069

5.3. Over-Voltage

In over-voltage conditions the grid voltage is increased 50% of its rated value for 200 ms from 1 s to 1.2 s as shown in Figure 10b. The V_{dc} of the proposed controllers is robust, faster, and stable soon after the grid voltage recovers as shown in Figure 10a. I_d for the PI, API and PR+RHC control controllers are clearly depicted in Figure 10c–e which prove that the proposed controllers are exactly following the reference value. Due to adaptiveness of the API and harmonic compensation of PR+RHC, both controllers are less sensitive to faults and the response is faster. I_r are also depicted in Figure 10f for all controllers. In case, the I_g responses in the API and PR+RHC controllers are fast and attain stability quickly after 1.2 s as shown in Figure 10g. Similarly I_q, the API and PR+RHC controller responses are fast and achieve stability soon after 1.2 s, while the PI controller responds after 1.5 s as elaborated in Figure 10h. The proposed controllers' responses in the case of P_r and P_s is less oscillatory and stable, which ensures stable performance is shown in Figure 10i,j. The proposed controllers' performances in the case of Ps_{react}, T_{em} and V_r are also dominant and less harmonic as shown in Figure 10k–m. Finally, THD of I_g is calculated, which is 1046.10% using the PI controller while it reduces to 446.52% and 684.51% in the case of the API and PR+RHC controllers which makes the proposed controllers more reliable and efficient in over-voltage conditions as shown in Figure 10n–p. The performance indices of all the control schemes are evaluated in Tables 8–10 for V_{dc}, I_d, and I_q, respectively. In the case of the API and PR+RHC controllers, all three parameters values are minimum compared with the PI controller, which validates the better performance of the proposed controllers.

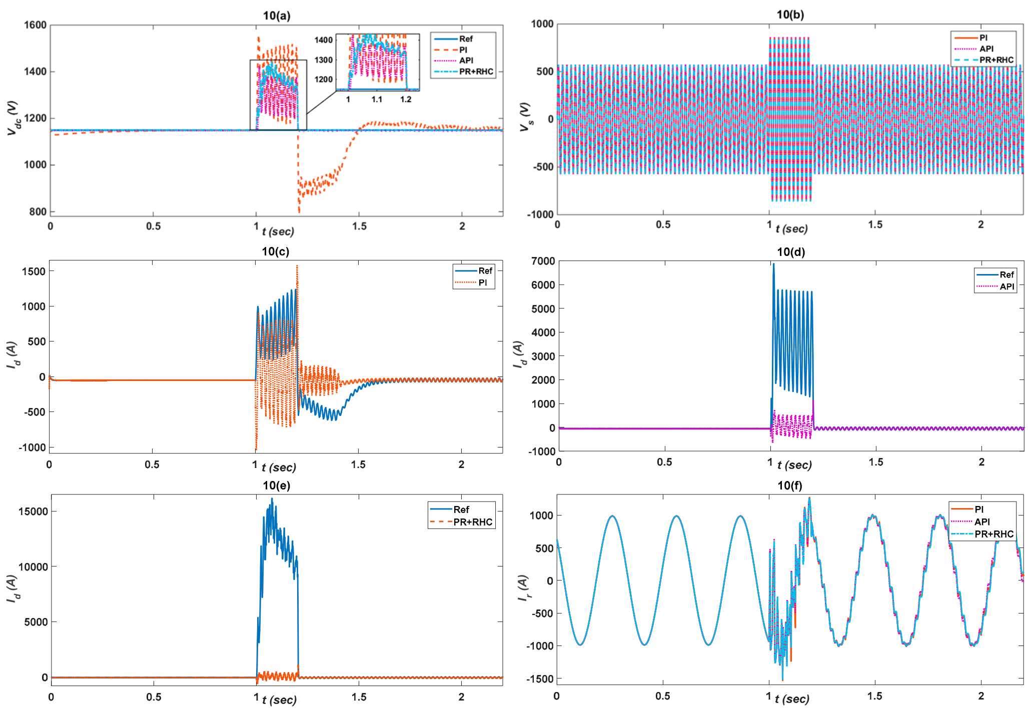

Figure 10. *Cont.*

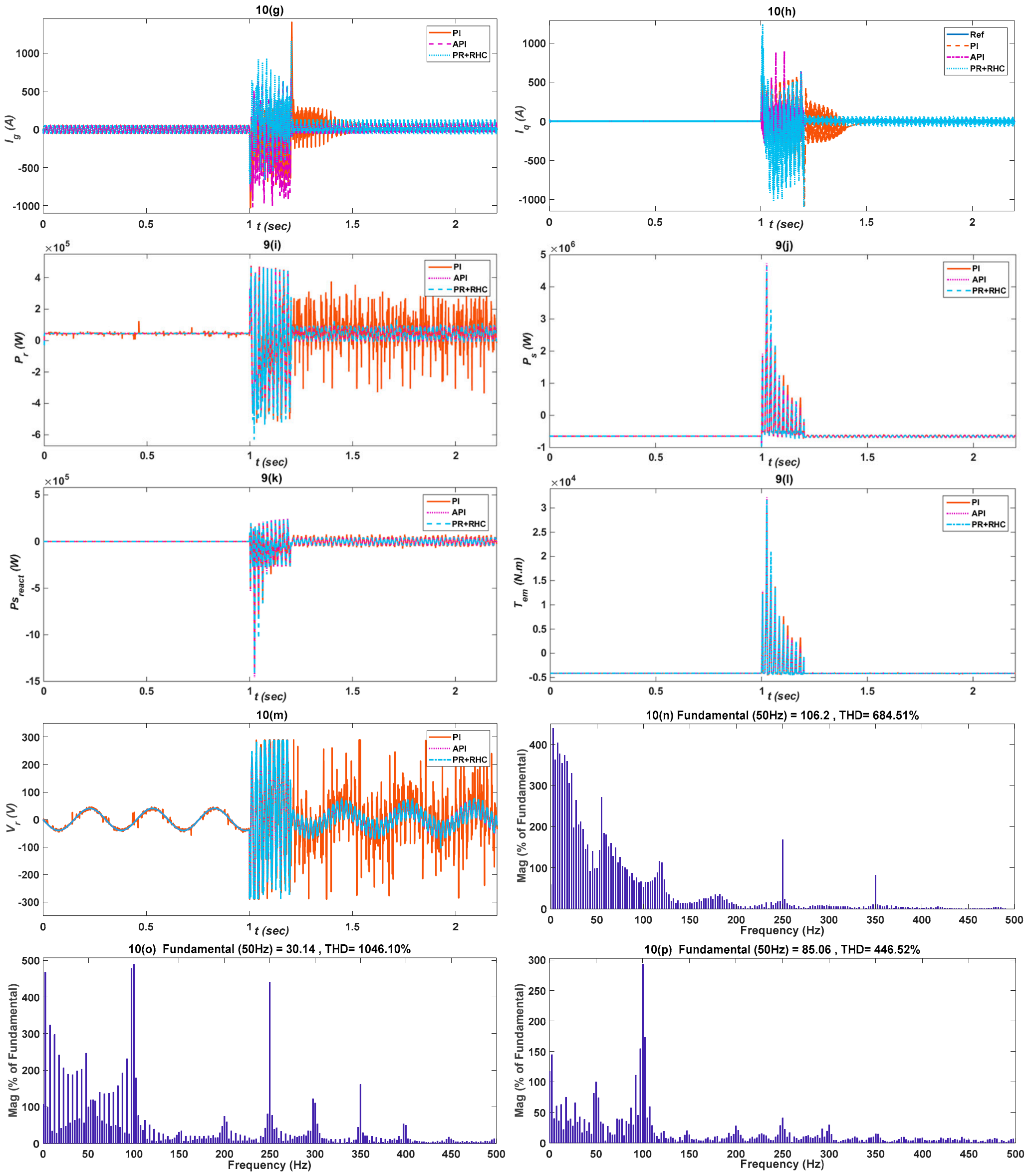

Figure 10. Comparison of PI and Proposed API and PR+RHC controller responses under overvoltage fault, considering: (**a**) Dc-link voltage V_{dc}; (**b**) Stator voltage V_s; (**c–e**) Active component of current I_d; (**f**) Rotor current I_r; (**g**) Reactive current component I_q; (**h**) Grid current I_g; (**i**) Rotor active power P_r; (**j**) Stator active power P_s; (**k**) Electromagnetic torque T_{em}; (**l**) Stator reactive power Ps_{react}; (**m**) Rotor voltage V_r; (**n**) PR+RHC controller THD; (**o**) PI controller THD; (**p**) API controller.

Table 8. Performance evaluation of the designed control strategies for V_{dc}.

Control Strategies	Performance Index		
	IAE	ISE	ITAE
PI	55.17	23.86	70.02
API	10.49	4.09	15.63
PR+RHC	14.49	6.89	9.02

Table 9. Performance evaluation of the designed control strategies for I_d.

Control Strategies	Performance Index		
	IAE	**ISE**	**ITAE**
PI	5.6	35.26	7.65
API	2.6	16.32	3.27
PR+RHC	3.1	15.36	4.09

Table 10. Performance evaluation of the designed control strategies for I_q.

Control Strategies	Performance Index		
	IAE	**ISE**	**ITAE**
PI	73.01	63.86	88.97
API	36.73	20.71	55.23
PR	35.29	19.06	49.74

5.4. Single Phase Fault

A single-phase fault is applied to evaluate the performance of the proposed controllers. The fault is applied for 200 ms from 1 s to 1.2 s as depicted in Figure 11b. The V_{dc} responses of the API and PR+RHC controllers are robust and attain stability soon after the fault is cleared, while the PI controller response is oscillatory and delayed in accomplishing stability after the fault is cleared as illustrated in Figure 11a. The I_d responses for the PI, API and PR+RHC controllers are shown in Figure 11c–e. The API controller updates its parameters using fuzzy rules to track the reference abruptly and the PR+RHC controller, due to its harmonic compensation, effectively minimizes the error, in comparison to the PI controller. I_r values for the conventional and proposed controllers are illustrated in Figure 11f. The I_q and I_g responses of the proposed controllers are more stable and less oscillatory as shown in Figure 11g,h. The responses of P_s and P_r powers, T_{em}, Ps_{react}, and V_r are shown in Figure 11i–m. Analyzing the controllers on the basis of the grid current I_g THD values, it clearly shows that the proposed API controller with 55.43% THD and PR+RHC with 60.91% THD show less harmonics with respect to the 76.35% THD of the PI controller with increased harmonics which shows that the proposed controllers' responses in case of a single-phase fault are robust and stable as compared to the PI controller as shown in Figure 11n–p. The performance indices of all the control schemes are evaluated in Tables 11–13 for V_{dc}, I_d, and I_q, respectively. In the case of proposed API and PR+RHC controllers, all three parameter values are minimum compared with the PI controller, which guarantees the better performance of the proposed controllers under single-phase fault conditions.

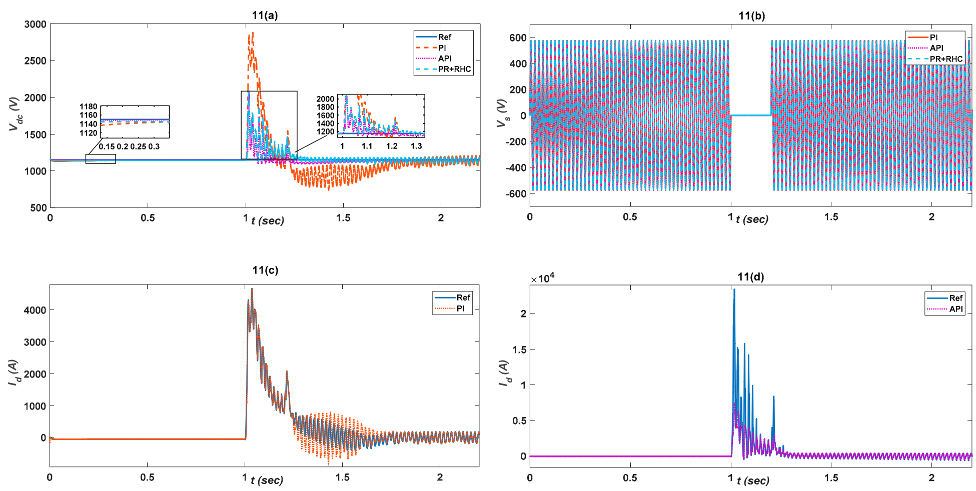

Figure 11. *Cont.*

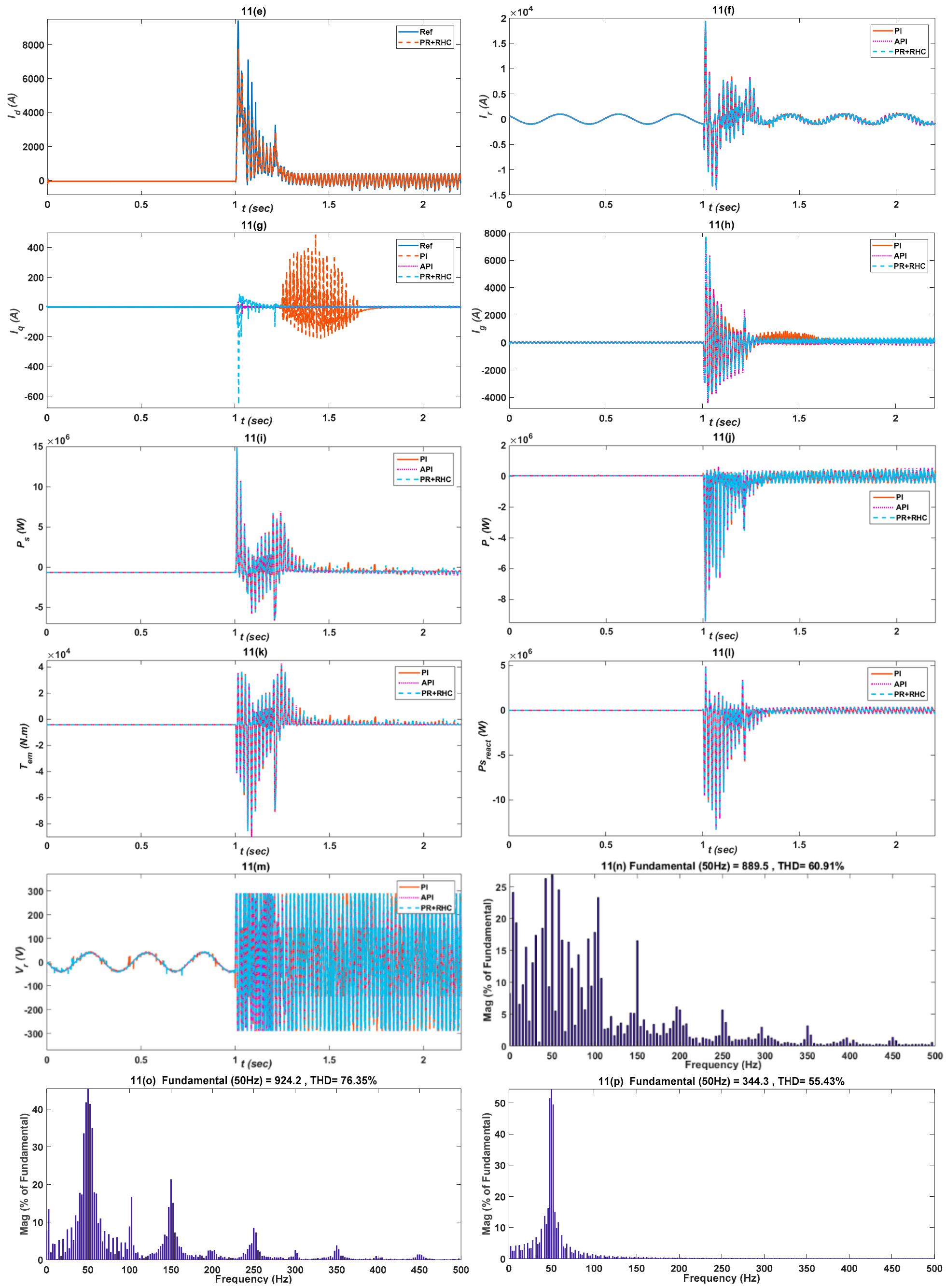

Figure 11. Comparison of PI and Proposed API and PR+RHC controller responses under Single-phase fault, considering: (**a**) Dc-link voltage V_{dc}, (**b**), Stator voltage V_s, (**c–e**) Active component of current I_d, (**f**) Rotor current I_r, (**g**) Reactive component I_q, (**h**) Grid current I_g, (**i**) Stator active power P_s, (**j**) Rotor active power P_r, (**k**) Electromagnetic torque T_{em}, (**l**) Stator reactive power Ps_{react}, (**m**) Rotor voltage V_r, (**n**) PR+RHC controller THD, (**o**) PI controller THD, (**p**) API controller.

Table 11. Performance evaluation of the designed control strategies for V_{dc}.

Control Strategies	Performance Index		
	IAE	**ISE**	**ITAE**
PI	366.1	63.23	754.1
API	80.64	32.36	170.7
PR+RHC	84.64	39.36	111.7

Table 12. Performance evaluation of the designed control strategies for I_d.

Control Strategies	Performance Index		
	IAE	ISE	ITAE
PI	190.4	5.323	35.5
API	0.20	1.916	0.25
PR+RHC	1.06	3.09	2.36

Table 13. Performance evaluation of the designed control strategies for I_q.

Control Strategies	Performance Index		
	IAE	ISE	ITAE
PI	45.59	456	73.66
API	11.58	154	15.51
PR+RHC	15..69	93	29.6

5.5. Two-Phase Faults

A two-phase fault is applied to evaluate the performance of the control strategies. The fault is applied for 200 ms from 1 s and cleared at 1.2 s, as shown in Figure 12b. The V_{dc} responses of the API and PR+RHC controllers are more stable, quickly tracking the reference value after the fault is cleared, as compared to the unstable response of the PI controller as presented in Figure 12a. A comparison of the I_d of all controllers (Figure 12c–e) indicates that the API and PR+RHC controllers clearly track the reference value while PI goes unstable as it proceeds after 1.2 s. The API controller employs fuzzy rules adoptively with robust response and the PR+RHC due to its harmonic compensation effectively minimizes the error, in comparison to the PI controller. Figure 12f describes the I_r responses for all the controllers. Similarly, the I_q and I_g responses are more stable and robust in the API and PR+RHC controllers' case as elaborated in Figure 12g,h. The responses of other parameters of WTs i.e., P_s, P_r, T_{em}, Ps_{react} and V_r are shown in Figure 12i–m. The grid current I_g THDs of all controllers are presented in Figure 12n–p.

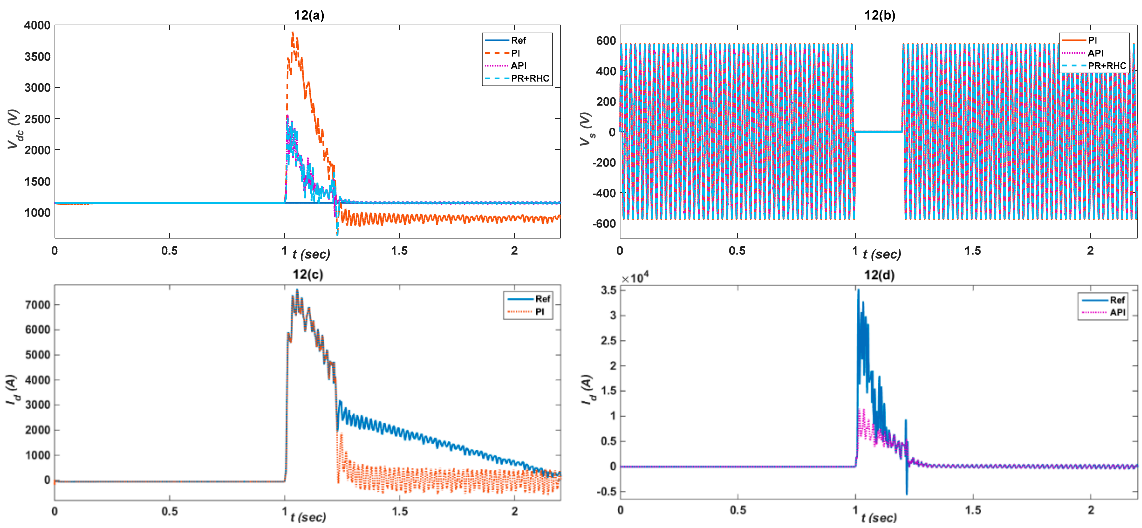

Figure 12. *Cont.*

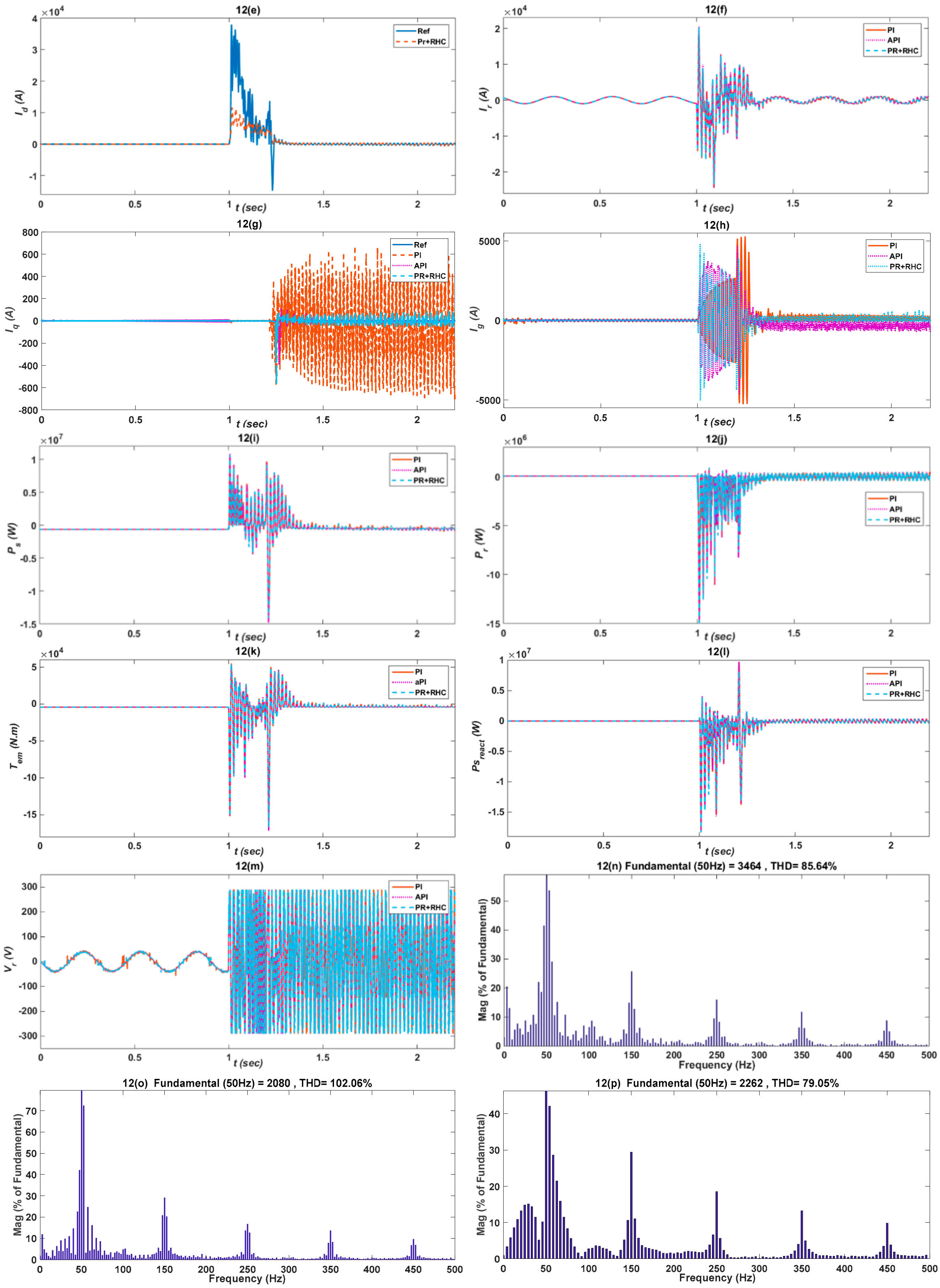

Figure 12. Comparison of PI and Proposed API and PR+RHC controller responses under two-phase fault, considering: (**a**) Dc-link voltage V_{dc}, (**b**) Stator voltage V_s, (**c–e**) Active component of current I_d, (f) Rotor current I_r, (**g**) Reactive component I_q, (**h**) Grid current I_g, (**i**) Rotor active power P_r, (**j**) Stator active power P_s, (**k**) Electromagnetic torque T_{em}, (**l**) Stator reactive power Ps_{react}, (**m**) Rotor voltage V_r, (**n**) PR+RHC controller THD, (**o**) PI controller THD and (**p**)API controller.

The API and PR+RHC controllers have THDs of 79.03% and 85.64% while the PI controller has 102.06% THD which demonstrates the effectiveness and dominance of the proposed (API & PR+RHC) controllers over PI. The performance indices of all the control schemes (PI, API & PR+RHC) are evaluated in Tables 14–16 for V_{dc}, I_d, and I_q, respectively. In the case of the proposed (API & PR+RHC) controllers, all three parameter values are minimum compared with the PI controller, which authenticates the better performance of the proposed controllers under two-phase fault conditions.

Table 14. Performance evaluation of the designed control strategies for V_{dc}.

Control Strategies	Performance Index		
	IAE	ISE	ITAE
PI	96.39	12.36	96.4
API	24.4	2.36	35.32
PR+RHC	29.31	3.59	39.85

Table 15. Performance evaluation of the designed control strategies for I_d.

Control Strategies	Performance Index		
	IAE	ISE	ITAE
PI	65.75	37.77	51.23
API	9.32	13.26	17.34
PR+RHC	14.60	19.32	24.09

Table 16. Performance evaluation of the designed control strategies for I_q.

Control Strategies	Performance Index		
	IAE	ISE	ITAE
PI	59.32	16.96	86.36
API	15.30	6.32	19.32
PR+RHC	20.96	9.96	24.49

6. Conclusions

Dynamic behaviors and critical issues like the stability of DC-link capacitor voltage and grid injected active and reactive power in DFIG-based WTs under voltage sags and grid faults were investigated and robust and novel Adaptive Proportional Integral (API) and Proportional Resonant with Resonant Harmonic Compensator (PR+RHC) controllers were proposed. The proposed DC-voltage control method is implemented independent of rotor side control which mitigates voltage harmonics in DC-capacitors and stabilizes active and reactive power which results in enhanced reliability of DC-link capacitor, WT stability, and makes control systems adoptable for large scale DFIG converters.

The performance of the PI control scheme shows sensitivity, large oscillations, and slow convergence to normal and abnormal conditions as verified from our simulation results, Total Harmonic Distortion (THD) analysis, and performance indices tables (Integral Absolute Error (IAE), Integral Square Error (ISE) and Integral Time-weighted Absolute Error (ITAE). However, comparatively the proposed controllers, i.e., API and PR+RHC, provide a better dynamic response, less sensitivity, fast convergence, less oscillation, robust, ripple-free and fault tolerant performance under normal and abnormal conditions.

Author Contributions: I.K., K.Z. and W.U.D. propose the main idea of the paper. I.K. implements the mathematical derivations, simulation verifications and analyses. The paper is written by I.K., and is revised by K.Z., W.U.D., S.U.I., M.I., S.H. and H.-J.K. All the authors were involved in preparing the final version of this manuscript. Besides, this whole work was supervised by H.-J.K.

Acknowledgments: This Research was supported by BK21PLUS, Creative Human Resource Development Program for IT Convergence.

Conflicts of Interest: The authors declare no conflict of interest.

Appendix A

Table A1. Model nominal parameters.

Generator Parameters	Values	Back-to-Back Converter	Data
Rated grid Power	2MW	Parallel converters	2
Polar pairs	2	Rated active power	400 kW
Gear ratio	95	DC-link voltage	1150 V
Rated shaft speed	1800 rpm	Switching frequency	2 kHz
Stator leakage inductance	0.038 mH	*Grid-side converter*	
Magnetizing inductance	2.91 mH	Rated output voltage	704 V
Rotor Leakage inductance	0.034 mH	Filter inductance	0.5 mH
Stator/rotor turns ratio	0.369	*Generator-side converter*	
		Rated output voltage	560 V

Table A2. Control schemes constants.

Control Schemes	Parameters	V_{dc}	I_d	I_q
PI	k_p	2.5	1.09	1.09
	k_i	10	17.25	17.25
API	k_p	25	250	250
	k_h	27500	200	200
PR+RHC	k_p	0.001	28	28
	k_i	0.01	1.5	1.5
	k_i^3 3rd	2	1.2	1.2
	k_i^5 5th	8	10	10
	k_i^7 7th	10	90	90

References

1. International Energy Agency. Wind Energy Technology Roadmap. 2009. Available online: http://www.iea.org/ (accessed on 22 November 2018).
2. Kaldellis, J.K.; Zafirakis, D. The wind energy revolution: a short review of a long history. *Renew. Energy* **2011**, *36*, 1887–1901. [CrossRef]
3. Abdeddaim, S.; Betka, A. Optimal tracking and robust power control of DFIG wind turbine. *Electr. Power Energy Syst.* **2013**, *49*, 234–242. [CrossRef]
4. Pena, R.; Clare, J.C.; Asher, G.M. Doubly fed induction generator using back-to-back PWM converters and its application to variable-speed wind-energy generation. *IEE Proc. Electr. Power Appl.* **1996**, *143*, 231–241. [CrossRef]
5. Ekanayake, J.B.; Holdsworth, L.; Wu, X.; Jenkins, N. Dynamic modeling of doubly fed induction generator wind turbines. *IEEE Trans. Power Syst.* **2003**, *18*, 803–809. [CrossRef]
6. Hu, J.; He, Y. DFIG wind generation systems operating with limited converter rating considered under unbalanced network conditions-analysis and control design. *Renew. Energy* **2011**, *36*, 829–847. [CrossRef]
7. Muljadi, E.; Yildirim, D.; Batan, T.; Butterfield, C.P. Understanding the unbalanced-voltage problem in wind turbine generation. In Proceedings of the 1999 IEEE Industry Applications Conference: Thirty-Forth IAS Annual Meeting, Phoenix, AZ, USA, 3–7 October 1999; pp. 1359–1365. [CrossRef]
8. Abad, G.; Lopez, J.; Rodriguez, M.; Marroyo, L.; Iwanski, G. *Doubly Fed Induction Machine: Modeling and Control for Wind Energy Generation Applications*; Wiley-IEEE Press: Hoboken, NJ, USA, 2011.
9. Yi, Z.; Bauer, P.; Ferreira, J.A.; Pierik, J. Operation of grid-connected DFIG under unbalanced grid voltage condition. *IEEE Trans. Energy Convers.* **2009**, *24*, 240–246.

10. Tazil, M.; Kumar, V.; Bansal, R.C.; Kong, S.; Dong, Z.Y.; Freitas, W.; Mathur, H.D. Three-phase doubly fed induction generators: An overview. *IET Electr. Power Appl.* **2010**, *4*, 75–89. [CrossRef]
11. EPCOS. Aluminum Electrolytic Capacitors General Technical Information. 2010. Available online: http://www.epcos.com (accessed on 24 November 2018).
12. Hitachi AIC. Aluminum Electrolytic Capacitors. 2011. Available online: http://www.hitachi-aic.com (accessed on 1 December 2018).
13. Song, H.; Nam, K. Dual current control scheme for PWM converter under unbalanced input voltage conditions. *IEEE Trans. Ind. Electron.* **1999**, *46*, 953–959. [CrossRef]
14. Xu, L. Coordinated control of DFIG's rotor and grid side converters during network unbalance. *IEEE Trans. Power Electron.* **2008**, *23*, 1041–1049.
15. Xu, L.; Wang, Y. Dynamic modeling and control of DFIG-based wind turbines under unbalanced network conditions. *IEEE Trans. Power Syst.* **2007**, *22*, 314–323. [CrossRef]
16. Pena, R.S.; Cardenas, R.J.; Clare, J.C.; Asher, G.M. Control strategies for voltage control of a boost type PWM converter. In Proceedings of the 2001 IEEE 32nd Annual Power Electronics Specialists Conference, Vancouver, BC, Canada, 17–21 June 2001; pp. 730–735. [CrossRef]
17. Malesani, L.; Rossetto, L.; Tenti, P.; Tomasin, P. AC/DC/AC PWM converter with reduced energy storage in the dc link. *IEEE Trans. Ind. Appl.* **1995**, *31*, 287–292. [CrossRef]
18. Liu, C.; Huang, X.; Chen, M.; Xu, D. Flexible control of dc-link voltage for doubly fed induction generator during grid voltage swell. In Proceedings of the 2010 IEEE Energy Conversion Congress and Exposition, Atlanta, GA, USA, 12–16 September 2010; pp. 3091–3095. [CrossRef]
19. Yao, J.; Li, H.; Liao, Y.; Chen, Z. An improved control strategy of limiting the dc-link voltage fluctuation for a doubly fed induction wind generator. *IEEE Trans. Power Electron.* **2008**, *23*, 1205–1213.
20. Kim, H.S.; Mok, H.S.; Choe, G.H.; Hyun, D.S.; Choe, S.Y. Design of current controller for 3-phase PWM converter with unbalanced input voltage. In Proceedings of the 29th Annual IEEE Power Electronics Specialists Conference, Fukuoka, Japan, 18–21 May 1998; pp. 503–509. [CrossRef]
21. Vincenti, D.; Jin, H. A three-phase regulated PWM rectifier with online feedforward input unbalance correction. *IEEE Trans. Ind. Electron.* **1994**, *41*, 526–532. [CrossRef]
22. Aziz, A.; Shafiullah, G.M.; Stojcevski, A.; Mto, A. Participation of DFIG based wind energy system in load frequency control of interconnected multi generation power system. In Proceedings of the 2014 Australasian Universities Power Engineering Conference, Perth, WA, Australia, 28 September–1 October 2014; pp. 1–6. [CrossRef]
23. Chowdhury, M.A.; Shafiullah, G.M. SSR mitigation of series-compensated DFIG wind farms by a nonlinear damping controller using partial feedback linearization. *IEEE Trans. Power Syst.* **2018**, *33*, 2528–2538. [CrossRef]
24. Faried, S.O.; Unal, I.; Rai, D.; Mahseredjian, J. Utilizing DFIG-based wind farms for damping subsynchronous resonance in nearby turbine-generators. *IEEE Trans. Power Syst.* **2013**, *28*, 452–459. [CrossRef]
25. Huang, P.-H.; EI Moursi, M.S.; Xiao, W. Subsynchronous resonance mitigation for series-compensated DFIG-based wind farm by using two-degree-of-freedom control strategy. *IEEE Trans. Power Syst.* **2015**, *30*, 1442–1454. [CrossRef]
26. Leon, A.E.; Solsona, J.A. Sub-synchronous interaction damping control for DFIG wind turbines. *IEEE Trans. Power Syst.* **2015**, *30*, 419–428. [CrossRef]
27. Uddin, W.; Zeb, K.; Tanoli, A.; Haider, A. Hardware-based hybrid scheme to improve the fault ride through capability of doubly fed induction generator under symmetrical and asymmetrical faults. *IET Gener. Trans. Distrib.* **2017**, 200–206. [CrossRef]
28. Muller, S.; Deicke, M.; De Doncker, R.W. Doubly fed induction generator systems for wind turbines. *IEEE Ind. Appl. Mag.* **2002**, *8*, 26–33. [CrossRef]
29. Zeb, K.; Khan, I.; Uddin, W. A Review on Recent Advances and Future Trends of Transformerless Inverter Structures for Single-Phase Grid-Connected Photovoltaic Systems. *Energies* **2018**, *11*, 1968. [CrossRef]
30. Blaabjerg, F.; Lonel, D.M. Power Electronics and Control for Large Wind Turbines and Wind Farms. In *Renewable Energy Devices and System with Simulation in MATLAB and ANSYS*, 1st ed.; CRC Press Taylor & Francis Group: Boca Raton, FL, USA, 2017; pp. 194–195. ISBN 9781498765831.

31. Erdogan, N.; Henao, H.; Grisel, R. An improved methodology for dynamic modelling and simulation of electromechanically coupled drive systems: An experimental validation. *Sadhana* **2015**, *40*, 2021–2043. [CrossRef]
32. Errami, Y.; Maaroufi, M.; Ouassaid, M. Modelling and control strategy of PMSG based variable speed wind energy conversion system. In Proceedings of the 2011 International Conference on Multimedia Computing and Systems, Ouarzazate, Morocco, 7–9 April 2011; pp. 1–6. [CrossRef]
33. Kundur, P. *Power Systems Stability and Control*, 1st ed.; McGraw-Hill Education: New York, NY, USA, 1994.
34. Bose, B.K. *Modern Power Electronics and AC Drives*; Prentice-Hill Inc.: Upper Saddle River, NJ, USA, 2008.
35. Mohan, N. *Advance Electric Drives Analysis, Control and Modeling using Simulink*, 1st ed.; Wiley: Hoboken, NJ, USA, 2001; ISBN 978-1-118-91113-6.
36. Boemer, J.C.; Burges, K.; Zolotarev, P.; Lehner, J.; Wajant, P.; Fürst, M.; Brohm, R.; Kumm, T. Overview of German grid issues and retrofit of photovoltaic power plants in German for the prevention of frequency stability problems in abnormal system conditions of the ENTSO-E region continental Europe. In Proceedings of the 1st Solar International Workshop on Integration of Solar Power Systems, Aarhus, Denmark, 24 October 2011.
37. Ackermann, T.; Ellis, A.; Fortmann, J.; Matevosyan, J.; Muljadi, E.; Piwko, R.; Pourbeik, P.; Quitmann, E.; Sorensen, P.; Urdal, H.; et al. Code shift: Grid specifications and dynamic wind turbine models. *IEEE Power Energy Mag.* **2013**, *11*, 72–82. [CrossRef]
38. Yuan, X.; Merk, W.; Stemmler, H.; Allmeling, J. Stationary-Frame Generalized Integrators for Current Control of Active Power Filters with Zero Steady-State Error for Current Harmonics of Concern Under Unbalanced and Distorted Operating Conditions. *IEEE Trans. Ind. App.* **2002**, *38*, 523–532. [CrossRef]
39. Zeb, K.; Uddin, W.; Khan, M.A. A comprehensive review on inverter topologies and control strategies for Grid connected photovoltaic system. *Renew. Sustain. Energy Rev.* **2018**, *94*, 1120–1141. [CrossRef]